Chen *et al. Soft Sci.* **2025**, *5*, 6
DOI: 10.20517/ss.2024.56

Soft Science

Research Article

Open Access

Check for updates

Highly sensitive and robust soft tri-axial tactile sensors enabled by dual inductive sensing mechanisms

Si Chen[1], Su Li[1], Yiting Zheng[1], Brian Fong[2], Yizong Li[1], Penghao Dong[1], David Hwang[1], Shanshan Yao[1,*]

[1]Department of Mechanical Engineering, Stony Brook University, Stony Brook, NY 11794, USA.
[2]Department of Electrical and Computer Engineering, Stony Brook University, Stony Brook, NY 11794, USA.

Correspondence to: Prof. Shanshan Yao, Department of Mechanical Engineering, Stony Brook University, 161 Light Engineering, Stony Brook, NY 11794, USA. E-mail: shanshan.yao@stonybrook.edu.

How to cite this article: Chen, S.; Li, S.; Zheng, Y.; Fong, B.; Li, Y.; Dong, P.; Hwang, D.; Yao, S. Highly sensitive and robust soft tri-axial tactile sensors enabled by dual inductive sensing mechanisms. *Soft Sci.* **2025**, *5*, 6. https://dx.doi.org/10.20517/ss.2024.56

Received: 24 Oct 2024 **First Decision:** 29 Nov 2024 **Revised:** 14 Dec 2024 **Accepted:** 21 Dec 2024 **Published:** 18 Jan 2025

Academic Editors: Nae-Eung Lee, Dae-Hyeong Kim **Copy Editor:** Ting-Ting Hu **Production Editor:** Ting-Ting Hu

Abstract

Tri-axial tactile sensors that provide real-time information on both normal and shear forces are enabling technologies for tactile perception, which open up new possibilities in robotics, human-machine interfaces, environmental sensing, and health monitoring. Among tri-axial tactile sensors based on different mechanisms, inductive sensors possess good robustness against environmental contamination. Their low sensitivity to normal and shear loads, however, is a critical barrier. This work presents the rational design of soft inductive tri-axial tactile sensors that are capable of distinguishing static or dynamic normal and shear loads, with exceptional tactile sensitivity. Dual mechanisms of Biot-Savart law and Eddy current effect are explored to overcome the long-standing sensitivity issue. In addition, a hybrid coil with non-uniform spacing is designed to generate uniform magnetic fields, addressing the limitations of traditional uniform coils and significantly improving the sensor's tactile sensitivity. The picosecond pulsed laser scribing technique makes it possible to pattern silver nanowires into inductive coils with high fidelity. A porous compressible layer is adopted to enable adjustable sensitivity and sensing range to meet diverse application demands. Finally, the sensor is integrated between the user's leg and the orthosis, showcasing the sensor's capability for real-time monitoring of tri-axial forces and its robustness against environmental objects.

Keywords: Tri-axial tactile sensors, pressure sensing, shear sensing, soft electronics, silver nanowires

INTRODUCTION

Tactile sensors, which convert external forces into electrical signals, are crucial for advancements in robotics, human-machine interfaces, environmental sensing, and health monitoring[1-8]. For instance, recent work demonstrates the capability of detecting the location and pressure of touch events, which is vital for tactile intent recognition, tactile interactions, privacy protection, and precise spatial mapping[9-12]. In particular, by fusing in-sensor perception and computing frameworks, the signal dimensionality for achieving both tactile location and pressure perception was significantly reduced[10,11]. Meanwhile, tri-axial sensors that are capable of monitoring both pressure and shear forces are equally important. Tri-axial sensors provide critical information on the direction of applied forces in addition to the magnitude[13-15], essential for precise monitoring of tasks, identification of changes in contact states, and accurate measurement of contact forces[16,17].

Tactile sensors based on various sensing mechanisms have been developed to detect and differentiate between normal and shear forces. Among different sensing mechanisms, piezoelectric sensors are better suited for detecting dynamic (change or rate of change) loads than static loads[18-23]. Tri-axial resistive tactile sensors have been widely explored but often suffer from hysteresis and nonlinearity[24-27]. Capacitive tactile sensors are noted for low hysteresis, good linearity, and wide dynamic range. The sensing signals can be easily interfered with by environmental contaminants (e.g., oil, water, and dust) due to their sensitivity to both conductive and dielectric materials[8,16,28-30]. Magnetic field-based sensors are able to capture displacement-dependent magnetic field changes using Hall-effect sensor chips, which can be correlated with applied forces[24,31,32]. However, these sensors remain vulnerable to interferences from geomagnetic fields[33]. When integrated on curvilinear surfaces, such as human skin, the sensor should exhibit good stretchability[34]. While commercially available products, typically based on strain gauge technologies, can measure both normal and shear forces, their lack of stretchability makes it difficult to adapt to the nonplanar surface[35,36].

Inductive sensors represent another method for tri-axial tactile sensing. The Eddy current (EC) effect has been employed to develop inductive sensors for measuring both normal and shear forces[33,37]. EC sensors, widely explored for non-contact displacement measurements and non-destructive testing systems, possess exceptional stability in challenging environmental conditions, such as underwater, dirty, and construction sites[38,39]. In EC-enabled tactile sensors, a conductive target (e.g., aluminum sheets) is often incorporated to correlate displacements with measured inductance. Liquid metal was recently introduced as a conductive target to improve flexibility[40]. In addition to conductive target and EC effect, magnetic film or magnetic composites are also exploited to enable force-dependent magnetic field changes and therefore inductance changes. However, for all these inductive sensors, low sensitivity to both normal and shear sensing remains a critical barrier that needs to be addressed for their widespread applications.

In this work, we introduce soft and robust dual tri-axial tactile sensors (DTTS) that are capable of detecting static or dynamic normal and shear loads with high sensitivity and low hysteresis [Figure 1A-C]. Several strategies are explored to tackle the long-standing sensitivity issue of inductive sensors: (1) The sensor uniquely leverages both the Biot-Savart law and EC effects to overcome the limitations of traditional inductive sensors that rely on a single mechanism [Figure 1D, Supplementary Note 1, Supplementary Figure 1, and Supplementary Table 1]. This dual-mechanism design provides higher sensitivity to both normal and shear forces. To the best of our knowledge, dual-mechanism inductive sensors have rarely been explored; (2) Moreover, an optimized hybrid coil with non-uniform spacing is designed to generate uniform magnetic fields, dramatically improving the sensor's sensitivity to normal/shear loads. While hybrid coil designs have been explored in the wireless power transfer system, this is the first application of such a design in inductive

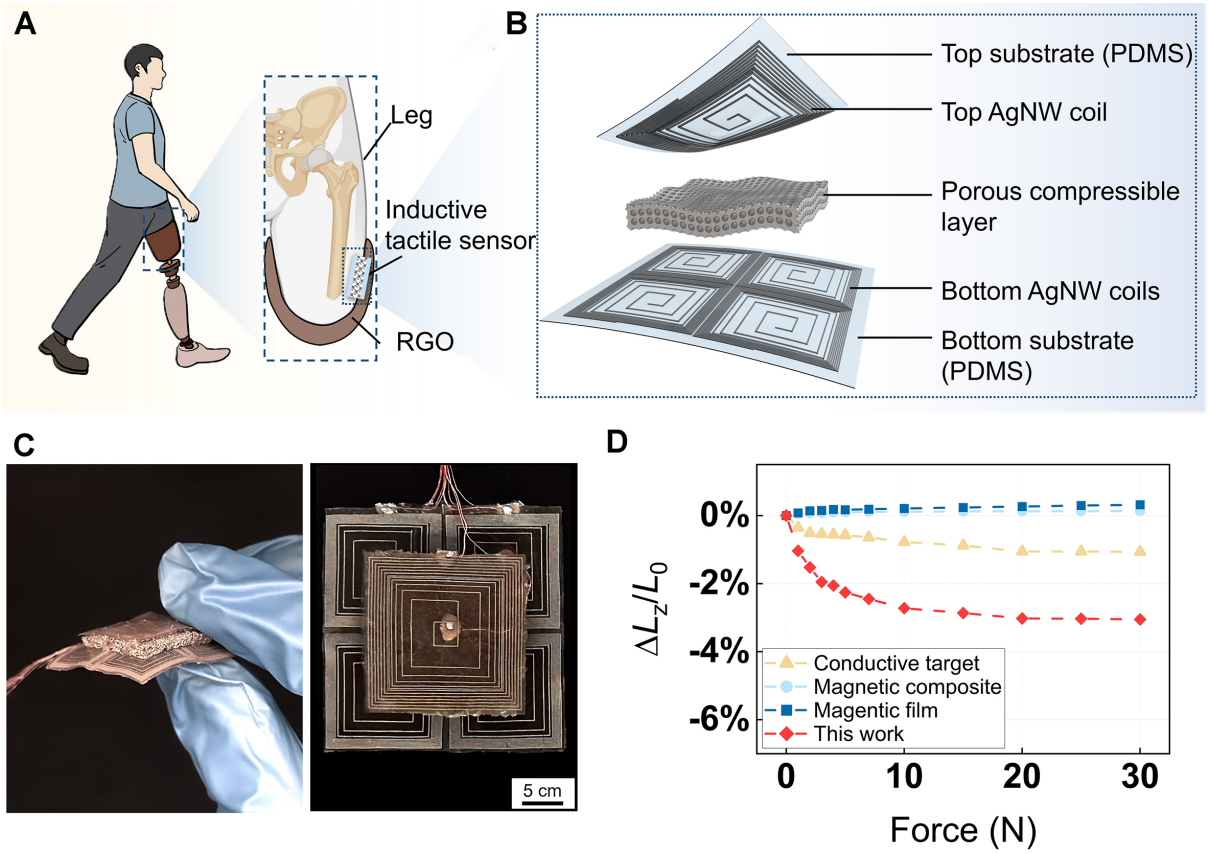

Figure 1. Overview of the DTTS. (A) One example of the application of the sensor in monitoring the normal and pressure loads between the leg and RGO; (B) Exploded-view schematic of the sensor; (C) Photograph of the sensor: (left) orthogonal-view; (right) top-view; (D) Performance comparisons between inductive tactile sensors based on different mechanisms. The geometry of the sensors is kept the same. Schematics and mechanisms of different types of inductive sensors are provided in Supplementary Note 2 and Supplementary Figure 2. Detailed material and fabrication process can be found in the Experimental section. ΔL_z represents inductance changes along the *z*-axis. L_0 represents the initial inductance of the sensor. DTTS: Dual tri-axial tactile sensors; RGO: reciprocating gait orthosis; PDMS: polydimethylsiloxane.

sensors to enhance sensitivity; (3) The sensor also incorporates a porous compressible layer (PCL). Introducing porous structures to the middle layer can greatly enhance tactile sensitivity. PCLs were fabricated through a droplet-based microfluidic assisted emulsion self-assembly method (DMAES), enabling highly ordered pore arrangement with precisely controllable sizes. This design allows for adjustable sensitivity and sensing range (from 2 kPa to 3.4 MPa) depending on the pore size, to meet diverse application demands. Incorporating silver nanowires (AgNWs) as the conductive materials for inductive coils enhances the flexibility and stretchability of the sensor, making it suitable for integration on nonplanar surfaces such as the human body. Employing a picosecond pulsed laser patterning technique, the coil can be fabricated with high precision, achieving a small line spacing of 40 μm. Finally, the sensor is integrated between the user's leg and an orthosis to demonstrate the sensor's capability for real-time tri-axial force monitoring and its stability against environmental objects.

In the results and discussion section, we present the materials and structures, tri-axial tactile sensing mechanisms, fabrication and optimization, and proof-on-concept demonstrations of the sensor. The fabrication and optimization subsection specifically addresses (1) the design methodology for the bottom and top coils to achieve uniform magnetic fields and optimized tactile sensing; (2) the fabrication and

optimization of the PCL, and finally; (3) the tactile sensing performance of the sensor.

EXPERIMENTAL

Materials

Polydimethylsiloxane (PDMS) (Dow Sylgard 184) was obtained from Ellsworth Adhesive. Ecoflex30 and Ecoflex gel were obtained from Smooth-On, Inc. Span 80, hexadecane, ethylene glycol (EG), polyvinylpyrrolidone (PVP, average Mw 360000), PVP (average Mw 55,000), iron (III) chloride ($FeCl_3$), silver nitrate ($AgNO_3$), N, N-dimethylformamide (DMF), and neodymium iron boron (NdFeB) were purchased from Sigma-Aldrich. All materials and reagents were used as received.

Fabrication process

AgNWs synthesis

AgNWs were synthesized using a modified polyol reduction method[41]. The PVP solution was prepared by dissolving 0.72 g PVP (Mw 55,000) and 0.72 g PVP (Mw 350,000) into 50 mL EG followed by magnetic stirring at 500 rpm and 100 °C until the PVP was fully dissolved. The $AgNO_3$ solution was prepared by dissolving 0.32 g $AgNO_3$ into 50 mL EG and stirring for 5 min at 500 rpm. Then, the PVP solution was heated to 150 °C in an oil bath. 10 mL $FeCl_3$ solution (600 μM in EG) was subsequently added to the PVP solution and stirred for 1 min at 500 rpm. The $AgNO_3$ solution was then added to the solution in the oil bath at a speed of 0.5 mL/min and stirred for 1 min. The solution was allowed to sit in the oil bath at 150 °C. After 2 h, the solution was cooled down to room temperature to stop the reaction. Finally, AgNWs were purified with acetone and ethanol, respectively. The solution was centrifuged three times at 2,000 rpm for 10 min to remove solvents, surfactants, and other impurities in the supernatant.

Laser patterning of AgNW coils

AgNW/ethanol solution was drop-casted on a glass substrate followed by evaporating the ethanol on a hot plate. Then, 0.7 g PDMS with a base-to-curing agent ratio of 10 : 1 was coated on the AgNWs using a spin coater (Laurell, WS-650Mz-23NPPB) at 700 rpm for 1 min, and thermally cured at 80 °C for 2 h. The PDMS film with AgNWs embedded inside was peeled off, flipped, and placed on a piece of glass substrate for laser patterning. A laser system consisting of a picosecond pulsed laser source (Photonics Industries, RG20H-532, 532 nm in wavelength, 100 kHz in firing frequency, around 12 ps in full-width-half-maximum temporal pulse width), a high-speed galvanometer scanning system (Scanlab, HurrySCAN//14), and an f-theta lens (Telecentric, focal length of 100 mm) was used for laser patterning. The laser beam was focused on the sample top surface with a beam spot diameter of around 20 μm (1/e definition), which is measured by Gaussian fitting of scribed feature sizes by varying laser powers[42]. After laser patterning, copper lead wires were attached to both the inner and outer terminals of the coil by the silver epoxy. Finally, a layer of PDMS was drop-casted to encapsulate the device, followed by thermal curing at 80 °C for 2 h.

Fabrication of PCL

The microfluidic droplet generators were constructed using a 3D-printed T-shaped reactor connected to the perfluoroalkoxy alkane tubing (outer diameter of 1/16 inches, inner diameter of 500 μm). The PDMS solution was prepared by mixing PDMS with a base-to-curing agent ratio of 10 : 1, hexadecane, and Span 80 in a weight ratio of 1 : 1: 0.03. This mixture was sonicated using a sonicator (Qsonica, Q500) at 500 W 20 kHz for 5 min and degassed for 30 min before use. To fabricate the PCL, volumetric flow rates of the deionized (DI) water and the PDMS solution were regulated by syringe pumps (Harvard Apparatus, PHD 2000 Infusion; Pum Systems Inc., NE-300 Just Infusion™ Syringe Pump). Water emulsion droplets in the PDMS solution were collected in a glass vial with a diameter of 4.5 cm and heated in an oven at 80 °C for 12 h, allowing the water to evaporate and the PDMS to cure. Subsequently, the sample was sequentially

immersed in ethanol, isopropyl alcohol, and DI water to remove the hexadecane and Span 80 residues thoroughly.

Inductive sensors based on different sensing mechanisms

For performance comparisons, the same AgNW/PDMS bottom coils were used for all sensors. The top layers, which can be a conductive film, magnetic film, or top coil for different sensors, were made identical in size, geometry, and position [more details in Supplementary Note 2]. The conductive film was fabricated by coating silver ink on a polyester (PET) film. The magnetic film was fabricated by mixing NdFeB microparticles with Ecoflex30 with a weight ratio of 3 : 5 and then coated onto a PET film. The material composition of the magnetic composite was the same as that of the magnetic film. Since the DMAES method cannot be used for magnetic composite, the porous structure within the magnetic composite was formed using a sugar sacrificial template method[43]. To ensure a fair comparison, a pure Ecoflex30 porous structure was inserted between the top coil, conductive film, magnetic film, and the bottom coils. The Young's Modulus of the pure Ecoflex30 porous structure is around 35 kPa. This pure Ecoflex30 porous structure matched the magnetic composite in both lateral dimension and height.

Characterizations

Stress-strain curves were measured using a material testing system (MTS, 858 Mini Bionix II). All PCL samples were applied with 70% compressive strain. The stress values were obtained by dividing the force by the cross-sectional area of the PCLs. The compressive strains were calculated by dividing the distance change by the original height of the PCL. All inductance values, except for those in the Applications section, were measured by an impedance analyzer (Keysight, E4990A). In the Applications section, the inductance values were obtained by an Inductance-to-Digital Converter (Texas Instruments, LDC1614). Capacitances of the capacitive sensors were measured by the same impedance analyzer (Keysight, E4990A). All displacements were obtained by a laser sensor (Keyence Corporation, IL-S025). Optical images were captured by a camera (Apple, iPhone 14). Microscopic images were acquired by a microscope (Evident, BX53M).

RESULTS AND DISCUSSION

Materials and structures

The sensor comprises three functional parts [Figure 1B]: the top coil, PCL, and four bottom coils, which are designed to enhance sensitivity through dual mechanisms [Figure 2A]. Top and bottom coils were fabricated by a selective laser patterning of thin AgNW layers embedded in a PDMS matrix. The top coil and the bottom four-coil array form a dual-layer planar coil configuration, which enables tri-axial tactile sensing based on the Biot-Savart law. PCL was made of porous PDMS embedded with conductive AgNWs, where highly ordered and adjustable porous microstructures were fabricated through a DMAES method[44]. Positioned between the dual-layer coils, the PCL (with AgNWs embedded) serves as a conductive medium (referred to as c-PCL hereafter) and interacts with top and bottom coils to generate EC. The sensor, constructed entirely from soft materials, demonstrates improved flexibility and wearability compared to other solutions for multi-axial inductive sensing[33,37,40,45].

Tri-Axial tactile sensing mechanisms

The inductance of a conductor (L) is given by:

$$L = \frac{1}{I}\iint B \cdot dA \tag{1}$$

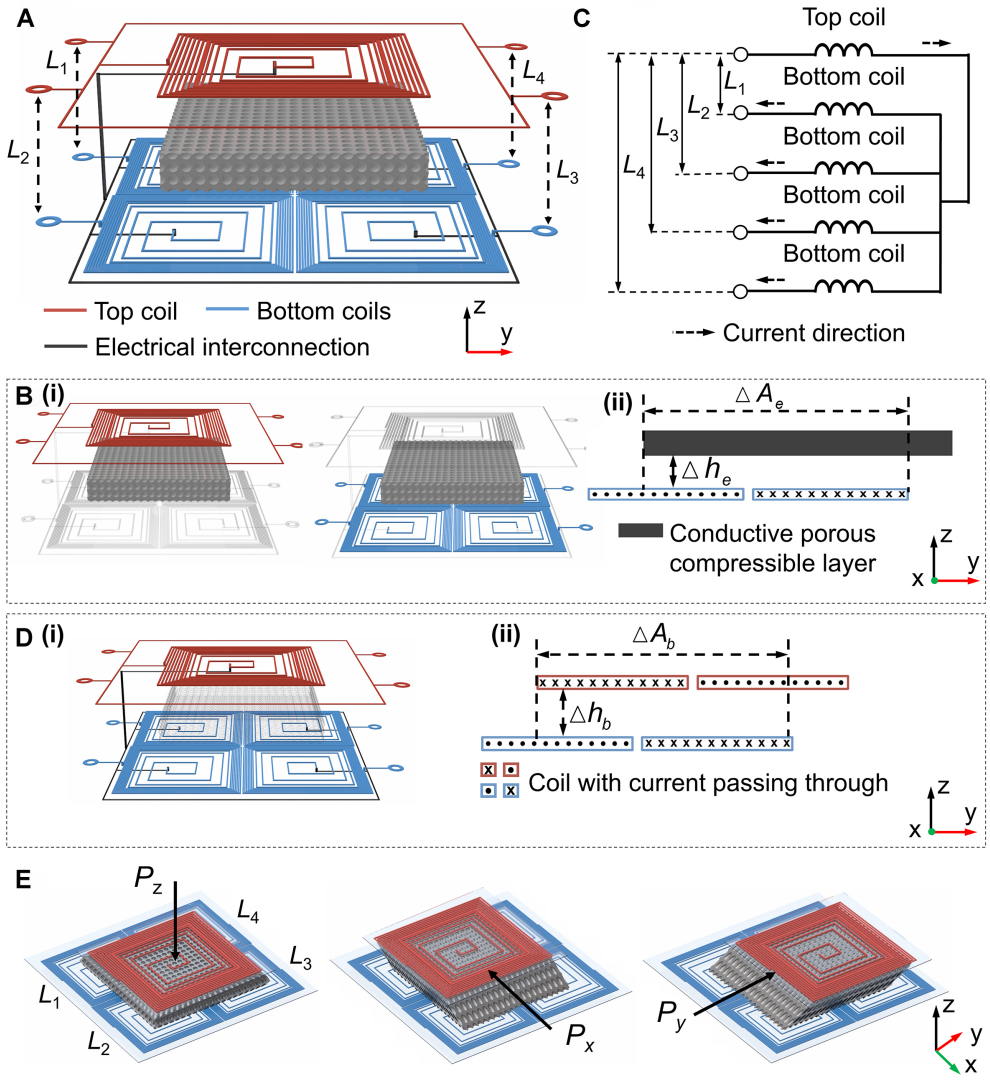

Figure 2. Structure and mechanisms of the DTTS. Structure of the DTTS: (A) Orthogonal-view schematic of the DTTS. L_1, L_2, L_3, and L_4 present the inductances of four dual-layer coils. The PDMS substrates for the top and bottom coils are not depicted; (B) Mechanism of the EC effect: (i) Interaction between (left) the c-PCL and the top coil; interaction between (right) the c-PCL and bottom coils, (ii) Cross-sectional view schematic of the relative movement between the c-PCL and one bottom coil. The legend of c-PCL represents the location of the central plane of c-PCL; (C) Circuit diagram showing the electrical interconnection between the top and bottom coils; (D) Mechanism of the Biot-Savart law: (i) Electrical connection of top and bottom coils, (ii) Cross-sectional view schematic of the relative movement between the top coil and one bottom coil; (E) Sensor deformations under normal and shear loads. P_x, $P_{y,\text{ and }}$ P_z present the loads along the x-, y-, and z-axis. DTTS: Dual tri-axial tactile sensors; PDMS: polydimethylsiloxane; EC: Eddy current; c-PCL: porous compressible layer (with AgNWs embedded) serving as a conductive medium.

If the current I is constant, L is proportional to the magnetic flux density B and the area A. The EC effect is commonly explored as the sensing mechanism of inductive tactile sensors. Activating a coil with an alternating current (AC) generates a magnetic field that further induces ECs in nearby conductive objects[46]. As the ECs produce a magnetic field that opposes the originally generated magnetic field from the coil, the magnetic flux density within the coil reduces, and so does the inductance of the coil[33,45]. More explanation of the EC effect is given in Supplementary Note 3.

In this work, as shown in Figure 2B, the c-PCL interacts with magnetic fields in the top coil and bottom coils. For simplicity in explaining the mechanism, only a single bottom coil is shown in Figure 2B (ii). Normal and shear loads induce the vertical and lateral movements of the c-PCL relative to the bottom coil. The displacements modulate the EC in the c-PCL and the magnetic field coupling between the c-PCL and coils due to the EC effect. Reducing the vertical distance (Δh_e) by the normal load increases the magnetic coupling between the c-PCL and bottom coils and reduces the inductance of the bottom coil. Conversely, reducing the lateral overlapping area (ΔA_e) by the shear load decreases the magnetic coupling and increases the inductance of the bottom coil[33]. However, due to energy dissipation, the magnetic field generated by the EC is weaker than the one produced by the coil[47]. Since the EC effect alone does not result in a significant reduction in coil inductance, sensors that rely solely on the EC effect cannot achieve a high sensitivity[33,37,40]. To enhance the sensitivity, this study leverages the Biot-Savart law in addition to the EC effect.

The inductance of a current-carrying wire (L_{wire}) is determined by the self-inductance (L_s) and mutual inductance (L_m)[48]:

$$L_{\text{wire}} = L_{\text{s}} + L_{\text{m}} \tag{2}$$

L_s is an inherent property of each current-carrying wire and varies with the wire's length and radius[49]. L_m occurs when two current-carrying wires are in proximity. When the wires are placed in parallel and the currents flow in the same direction, the magnetic flux density between the wires increases, enhancing the L_m. Conversely, if the currents flow in the opposite direction, the magnetic flux density between the wires decreases, thereby decreasing the L_m. A single-turn square coil can be divided into a four-segment current-carrying straight wire. The inductance of each wire segment should be calculated and added together to determine the inductance of the entire coil. Based on the Biot-Savart law, the generated magnetic flux density B at the center of a single-turn square coil arising from a current I can be calculated as[48]:

$$B = \frac{\sqrt{2}\mu_0 I}{\pi l} \tag{3}$$

where l is the radius of the coil and μ_0 is the vacuum permeability ($\mu_0 = 4\pi \times 10^{-7}\ N \cdot A^{-2}$). The detailed analytic calculation of the magnetic flux density generated by a single-turn square coil can be found in Supplementary Note 4.

In a dual-layer coil configuration, the vertical distance between top and bottom coils decreases under normal force and the lateral overlapping area decreases under shear force. In order to enhance the inductance changes caused by EC (i.e., inductance reduction under normal force or inductance increase under shear force), it is essential that wires in two layers carry opposite currents. Considering this requirement, the top coil is connected with each bottom coil in series to form four dual-layer coils where the wire segments of coils in two layers carry opposite currents [Figure 2C]. For simplicity, only one dual-layer coil was shown to illustrate the sensing mechanism [Figure 2D]. Under a normal load, the reduced distance (Δh_b) between the top and bottom coils leads to an enhanced interaction between the opposite magnetic fields from the top and bottom coils, giving rise to a reduction in the inductance. Whereas under a shear load, the reduced overlapping area (ΔA_b) reduces the magnetic interaction and increases the inductance. The influence of distance and overlapping area on the inductance by the Biot-Savart law is consistent with that by the EC effect. Employing both mechanisms magnifies the reduction in the coil inductance due to normal or shear loads, thereby achieving high sensitivity in tri-axial tactile sensing.

Considering the entire sensor with one top coil and four bottom coils, the inductances of four dual-layer coils can be presented as L_1, L_2, L_3 and L_4. When an external force is applied, the top coil is moved vertically (due to normal force) and laterally (due to the shear force) through the deformation of the c-PCL, resulting in changes in the inductance of four dual-layer coils [Figure 2E]. For example, when the top coil is pushed to move along the +*y*-axis due to the shear force, the overlapping area between the left two bottom coils and the top coil decreases, while the area between the right two bottom coils and the top coil increases. The changes in overlapping areas further lead to increased L_1 and L_2, but decreased L_3 and L_4. The same principle applies to the -*y*-axis and ±*x*-axes. In the following discussion, the displacement and load along the *y*-axis are used as an example of shear sensing. As for the *z*-axis, if the top coil is applied with normal force, the vertical distance between the top coil and bottom coils decreases, leading to the decrease of L_1, L_2, L_3 and L_4. Due to the symmetric configuration of the sensor, the inductances in response to displacements (*dx, dy, dz*) in the *x*-, *y*-, and *z*-axes are[33]:

$$\begin{cases} L_1(dx) = L_2(-dx) = L_3(-dx) = L_4(dx) \\ L_1(dy) = L_2(dy) = L_3(-dy) = L_4(-dy) \\ L_1(dz) = L_2(dz) = L_3(dz) = L_4(dz) \end{cases} \tag{4}$$

Based on the above analysis, the tri-axial tactile loads can be related to the following defined inductances along the *x*-, *y*-, and *z*-axes[40]:

$$\begin{cases} L_x = (L_1 + L_4) - (L_2 + L_3) \\ L_y = (L_1 + L_2) - (L_3 + L_4) \\ L_z = L_1 + L_2 + L_3 + L_4 \end{cases} \tag{5}$$

Fabrication and optimization

Laser-patterning of AgNW-based coils

Copper traces on flexible printed circuit boards (FPCBs) are commonly utilized as inductive coils in inductive tactile sensors. The applications of these sensors on nonplanar surfaces are limited due to the lack of stretchability[33,37,40,45,50,51]. To identify a more suitable conductive material for the coils, three materials were evaluated in this study: copper wires, silver ink, and AgNWs. Supplementary Figure 4 summarizes the inductance changes as a function of the displacement between the top coil and bottom coils for sensors based on three materials. The results reveal that the coil material does not significantly affect the sensor performance. AgNWs were selected as the coil material taking advantage of their superior mechanical compliance and excellent electrical conductivity[43,52]. For a comprehensive evaluation of the stretchability of these materials, please refer to Supplementary Note 5.

PDMS serves as the polymeric matrix for embedding AgNWs. The fabrication processes of AgNW/PDMS coils are illustrated in Figure 3A. To start, a shadow mask was prepared and secured onto a glass substrate. AgNW/ethanol solution was drop-casted over the mask followed by evaporating the solvent. Following the removal of the mask, a PDMS solution was spin-coated over the AgNW networks and thermally cured. This process embedded the AgNWs just below the surface of the PDMS matrix (around 10 μm depth), enabling an electrode architecture of enhanced electromechanical stability under mechanical deformation. More details of fabrication processes can be found in the Experimental section. Subsequently, the AgNW/PDMS film was peeled off, flipped (with the AgNW surface facing up), and positioned on a glass substrate for laser patterning into the top and bottom coils in high precision. After this, lead wires were attached to the two ends of the coils [not depicted in Figure 3A]. Another layer of PDMS was then spin-coated on the patterned coils and thermally cured to encapsulate the coils. Finally, the top and bottom AgNW/PDMS coils were sandwiched around the prepared c-PCL (discussed in the next section) to assemble the final tactile sensors.

A smaller line spacing of the coil provides two primary benefits: (1) It enables a more uniform magnetic field generated by the coil [more discussion can be found in Supplementary Notes 6 and 7, Supplementary

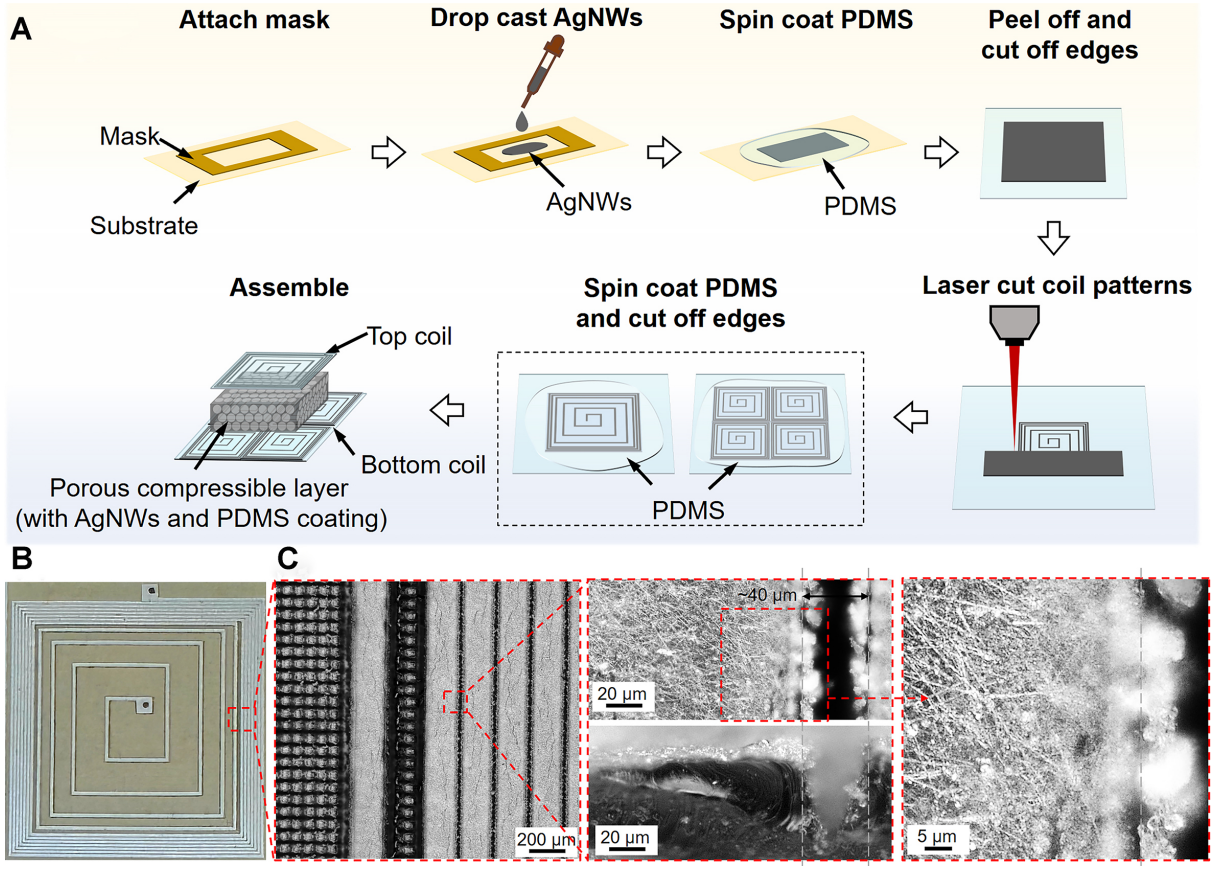

Figure 3. Fabrication processes of the sensor. (A) Schematic illustrations of the fabrication process of DTTS; (B) Photographic and (C) optical microscopic images of the laser-patterned AgNWs coil - the left, upper middle, and right images are top views of the fabricated AgNW coil patterns; the lower middle image is the cross-sectional view of a fabricated AgNW coil pattern. The laser-cutting width of around 40 μm by a single laser scan is marked in between dashed guidelines for cutting boundaries. For the AgNW coil patterns of large interspacing, multiple offset laser scribing paths are used to achieve electrical isolation with a minimal processing load, typically resulting in grid-like patterns in the left image in (C). DTTS: Dual tri-axial tactile sensors; PDMS: polydimethylsiloxane; AgNWs: silver nanowires.

Figure 8]; and (2) it increases the coil inductance, thereby improving the stability of inductance measurements and the signal to noise ratio of the tactile sensor. For a precise coil fabrication with small line spacing, we utilized a picosecond pulsed laser source with a firing frequency of 100 kHz, a wavelength of 532 nm, and a temporal pulse width of approximately 12 picoseconds in full width half maximum. Detailed discussions on the selection of laser-cutting parameters are provided in Supplementary Note 8. Compared to the previous work using traditional continuous laser for patterning AgNWs (with a patterning resolution of around 100 μm)[53,54], the picosecond pulsed laser utilized in this work significantly improves the patterning resolution (to around 40 μm) [Figure 3B and C].

Design of bottom AgNW coils for uniform magnetic field distribution and enhanced tactile sensing

For the bottom coils, two parameters were considered: (1) the number of coils and (2) the coil line spacing. Configurations with three or four coils are commonly used to develop tri-axial sensors [Supplementary Figure 9][33,37,40,55-57]. Compared to three-coil inductive sensors, the four-coil arrangement offers the advantage of an axially symmetric structure, typically a more linear response to lateral movements, and a larger inductance change in response to the tri-axial motion of the top coil[37]. Existing inductive sensors frequently utilize planar spiral coils with uniform line spacing as inductors [Figure 4A][33,37,39,40,45,58]. Nevertheless, the

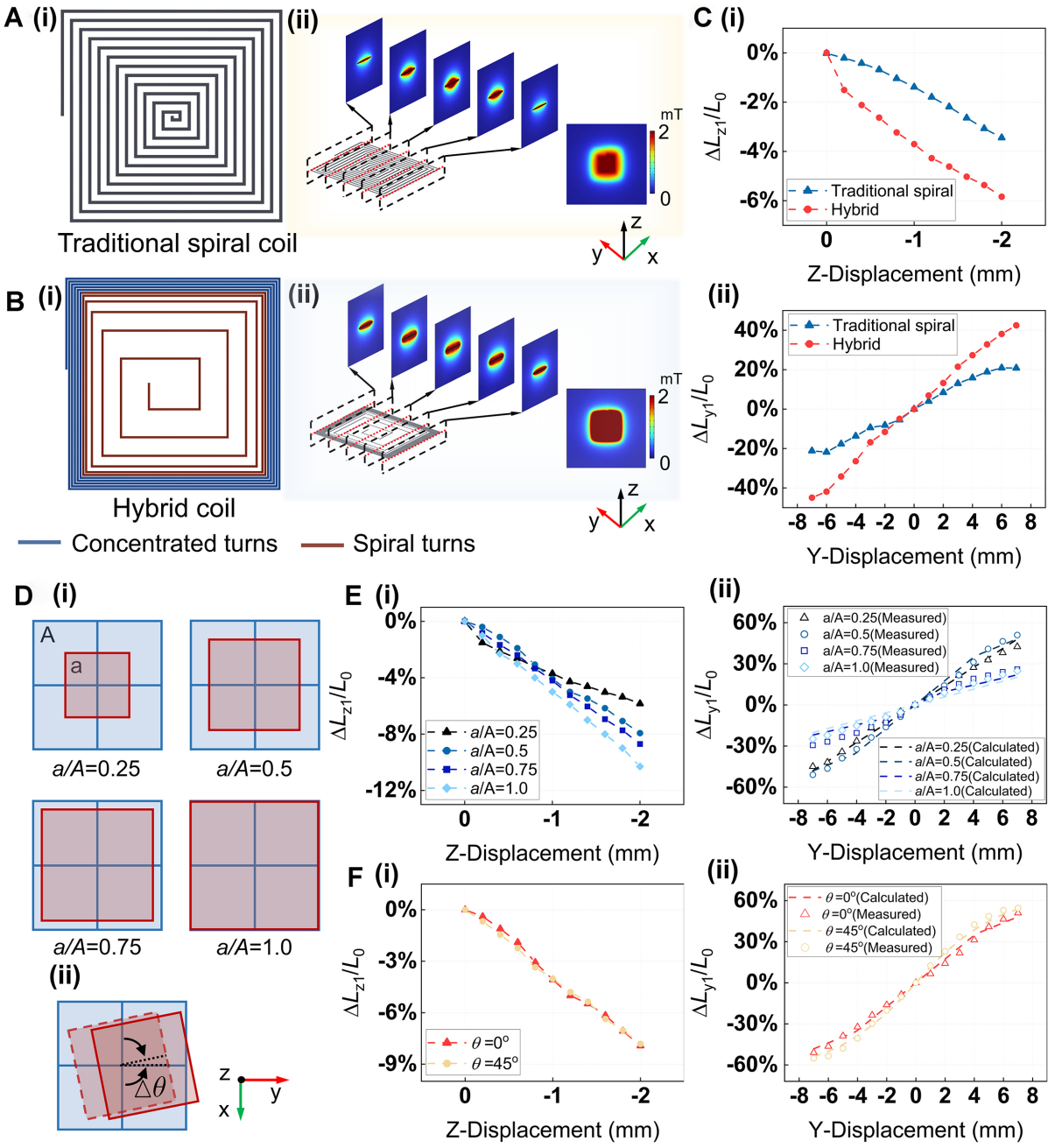

Figure 4. Optimization of coils. Magnetic flux density and performance of the traditional spiral coil (with uniform spacing) and the designed hybrid coils (with non-uniform spacing): (i) Patterns and (ii) simulation results of the magnetic flux density of (A) the traditional spiral and (B) the designed hybrid coil (k = 0.4). The right image in (ii) is the top-view magnetic flux densities for each type of coil; (C) Inductance changes as a function of displacements along the (i) z-axis and (ii) y-axis of tactile sensors based on different types of coils (a / A = 0.25). ΔL_{z1} and ΔL_{y1} represent changes of L_1 along the z-axis and y-axis, respectively; (D) Illustration of the (i) coverage ratio and (ii) orientation of the top coil (red) relative to the bottom coils (blue). "a" represents the area of the top coil, and "A" represents the total area of the bottom coils; (E) Sensing performance for different coverage ratios: (i) Measured inductance changes along the z-axis and (ii) measured and calculated inductance changes along the y-axis; (F) Sensing performance for different orientations of the top coil: (i) Measured inductance changes along the z-axis and (ii) Measured and calculated inductance changes along the y-axis.

uneven magnetic field generated by these coils negatively affects the sensitivity of the sensor's performance,

particularly in the lateral direction for shear sensing. As a result, enhancing the lateral sensitivity has become a crucial area of focus[33,37,40]. Since the relationship between inductance changes and displacements along the *x*-, *y*-, and *z*-axes has been discussed [Equations (4) and (5)], for simplicity, only L_1 was measured for the following optimization of top and bottom coils[32].

To improve the sensor's lateral shear sensing performance, a unique square planar coil was designed to generate a more uniform distribution of the magnetic field[37,47], which was inspired by the coil design in a wireless power transfer system. The coil adopts a hybrid structure consisting of outer concentrate turns and inner spiral turns, both positioned on the same plane [Figure 4B (i)][59]. The "concave" magnetic field distribution produced by the outer concentrated turns is effectively compensated by the "convex" magnetic field distribution from the inner spiral turns[60]. By optimizing parameters such as the number and spacing of turns, a more uniform magnetic flux distribution can be achieved[59,61,62]. More details on the design and optimization of the hybrid coil can be found in Supplementary Notes 6 and 7. The optimized hybrid coils employ an 11-turn coil configuration with five outer concentrated turns and six inner spiral turns. Magnetic flux densities of the designed hybrid coils were simulated using the COMSOL Multiphysics AC/direct current (DC) module. The result shows that the hybrid coil with non-uniform spacing can achieve a more uniform distribution of the magnetic field [Figure 4B (ii)] than the traditional spiral coil with uniform spacing [Figure 4A (ii)]. Tactile sensing performance along the *z*-axis and *y*-axis was evaluated to verify the effectiveness of the designed hybrid coils [Figure 4C]. As expected, sensors using the designed hybrid coils (with non-uniform spacing) achieve a higher sensitivity than those based on traditional spiral coils (with uniform spacing), particularly in the lateral direction for shearing sensing.

Design of the top AgNW coil for optimized tactile sensing

For the top coil, two parameters were evaluated: (1) the converge ratio and (2) the top coil orientation. To achieve an optimized tactile sensing performance, the magnetic flux density produced by the top coil should also be uniform and the interaction between the opposite magnetic fields from the top and bottom coils should be maximized. Here, the influence of the size and orientation of the top coil on the sensor performance was explored [Figure 4D]. To optimize the size of the top coil, the coverage ratio, defined as the top coil area to the total area of bottom coils (a / A), was varied from 0.25 to 1, while the orientation of the top coil was kept at $\Delta\theta = 0°$. For each coverage ratio, the number and spacing of turns of the top coil were designed to achieve a uniform magnetic flux density that matched the opposite magnetic flux density generated by the bottom coils. The patterns and simulation results for different coverage ratios can be found in Supplementary Figure 8. Figure 4E (i) shows that, for displacements along the *z*-axis under a normal force, the inductance decreases when the top coil moves closer to the bottom coils, and the inductance reduction is larger when the coverage ratio is larger. For displacements along the *y*-axis under a shear force, the inductance changes almost linearly with the overlapping area [Figure 4E (ii)], which is consistent with the calculated results [see Supplementary Note 9 for details], demonstrating the sensor's good predictability. When the coverage ratio is 0.5, the sensor exhibits the highest shear sensitivity. Considering the sensitivity for both normal and shear loads, when the coverage ratio increases from 0.5 to 1, the decrease in the shear sensitivity is more significant than the increase in normal force sensitivity. Thus, 0.5 was selected as the coverage ratio of the top and bottom coil.

Keeping the coverage ratio as 0.5 (a / A = 0.5), two orientations of the top coil ($\Delta\theta = 0°$, 45°) were explored. As illustrated in Figure 4F, the experimental results are consistent with the calculated results. Neither normal nor shear sensitivity shows significant dependence on the top coil orientation. Therefore, the optimal orientation for the top coil was selected as 0° with a coverage ratio of 0.5 relative to the total area of the bottom coils.

Fabrication and optimization of PCL

Existing inductive sensors in the literature have commonly employed solid polymers, such as Ecoflex and PDMS, as the middle layer to construct tactile sensors[33,37,45]. Introducing porous structures to the middle layer can greatly enhance tactile sensitivity. The fabrication method for creating PCL using DMAES is illustrated in Figure 5A[44]. Briefly, the PDMS solution composed of PDMS, hexadecane, and span 80 was prepared, as detailed in the Experimental section. The PDMS solution and DI water were allowed to flow through a perpendicularly arranged capillary tube using two syringe pumps and met at the T-junction. Here, DI water droplets were injected into the PDMS solution. Span 80 in the PDMS solution served as a surfactant that created steric barriers when it was absorbed in the water/PDMS interface[44]. This method prevents the water droplets from merging and guarantees structural stabilization[44]. After curing the PDMS, the DI water was evaporated, resulting in a 3D porous PDMS structure with uniform micropores [Supplementary Figure 11A as an example]. By controlling the flow rates of the DI water and PDMS solution, the pore size can be adjusted from 400 to 1,200 μm [Figure 5B].

To employ the EC effect for enhanced tactile sensing, AgNW coating was introduced to render the PCL conductive. The as-prepared PCL was dip-coated in an AgNW/ethanol solution, followed by solvent evaporation, as illustrated in Figure 5C. The coated PCL was then cut into the desired shape and subsequently dip-coated with a thin layer of Ecoflex30 for encapsulation to form the final c-PCL. This encapsulation not only prevents AgNWs from delaminating from the porous PDMS structure but also maintains reliable adhesion between the PCL and top/bottom coils, even under repetitive mechanical deformations. Four c-PCL samples with different pore sizes [0 (solid structure), 200, 500, and 750 μm] were evaluated for their elastic moduli. As shown in Figure 6A and Supplementary Figure 11B, increasing the pore size results in a higher porosity, lower density, and reduced elastic moduli of the c-PCL. The controllable elastic modulus enables customization of the c-PCL to meet the specific sensitivity and sensing range requirements for different applications. The effect of pore size on these sensing parameters is further detailed in Figure 6B and C. The results show that a larger pore size leads to a higher sensitivity but a reduced tactile sensing range. Pore size could be selected and customized based on the sensing requirements of different application scenarios. In this work, we explore the application of the sensor for monitoring the tactile loads between the user and the reciprocating gait orthosis (RGO) (discussed in the Applications section). Since arterial capillary pressure is 32 mm/Hg (around 4.3 kPa), a sustained pressure above these values can lead to tissue ischemia and necrosis[63,64]. To prevent pressure ulcers, the sensor should be able to measure normal and shear loads below 4.3 kPa. To achieve balanced sensing properties that meet the requirements of the RGO application, the c-PCL with a 500 μm pore size was chosen for further studies. A loading-unloading test was conducted to assess strain-stress curves under normal and shear loadings [Figure 6D and E], which indicates the good mechanical reliability of the c-PCL.

To evaluate the effectiveness of the c-PCL as a conductive medium to induce the EC, the performance of sensors with and without AgNWs was compared. As illustrated in Supplementary Figure 12, the sensor based on the c-PCL (with AgNWs) shows a larger inductance reduction compared to that based on non-conductive PCL (without AgNWs), especially for normal force sensing. The improvement in inductance changes and sensitivity is attributed to the EC effect. These results confirm that the developed DTTS sensors based on dual mechanisms (i.e., Biot-Savart law and the EC effect) exhibit enhanced sensitivity compared to those based on a single mechanism.

Tactile sensing performance of the DTTS

Figure 7A and B presents the inductance changes of the DTTS under various normal and shear loads with low hysteresis. As illustrated in Figure 7B, a highly linear relationship between the shear load along the

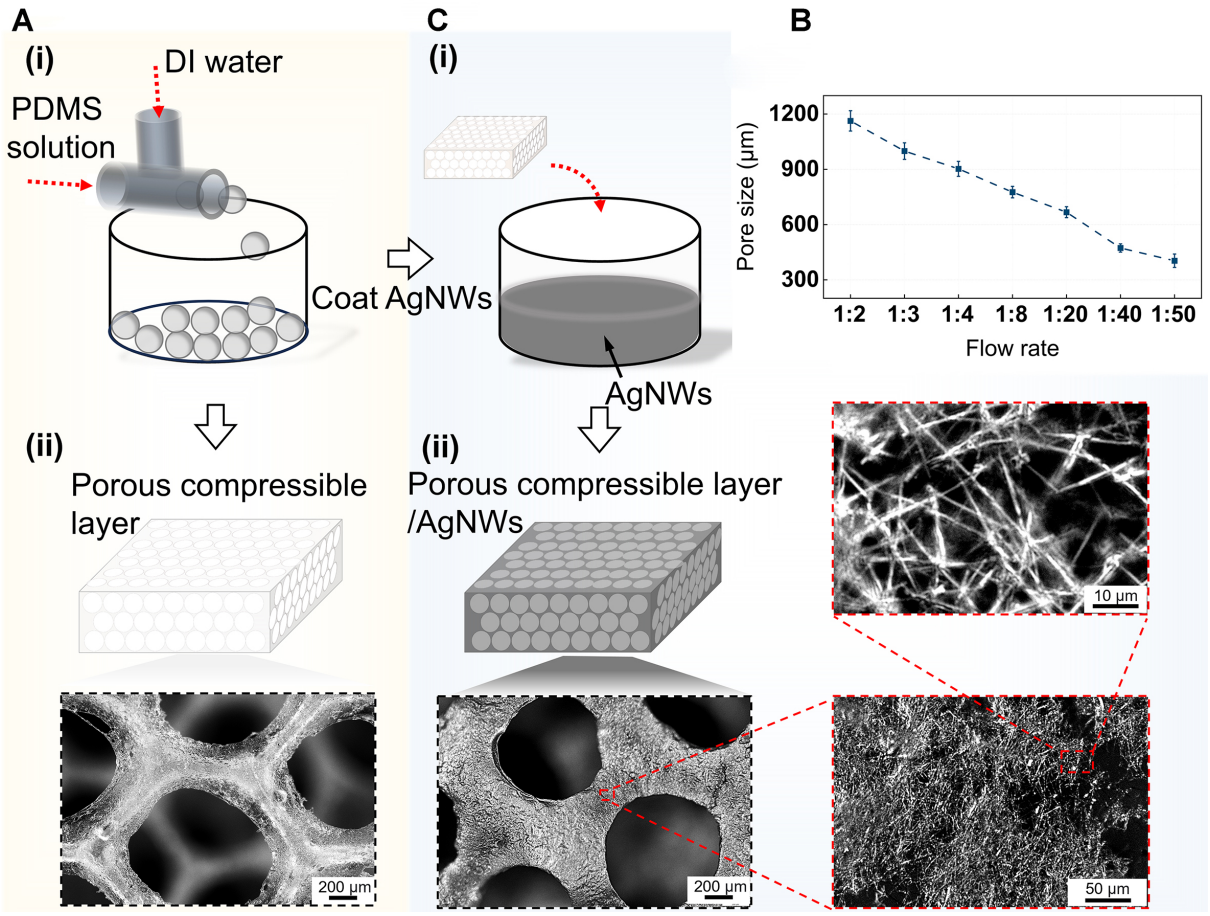

Figure 5. Fabrication process of PCL. (A) Fabrication method of PCL: (i) Schematic illustration of the generation of microdroplets; (ii) microscopic image of the PCL; (B) Relationship between the pore size and flow rate ratio of the DI water and PDMS solution. AgNW coating and encapsulation processes result in around 250 μm reduction of pore size; (C) Fabrication method of c-PCL: (i) Schematics of embedding AgNWs in the PCL, (ii) microscopic images of the c-PCL without encapsulation. The encapsulation process is not depicted. PDMS: Polydimethylsiloxane; AgNWs: silver nanowires; PCL: porous compressible layer; c-PCL: PCL (with AgNWs embedded) serving as a conductive medium; DI: deionized.

y-axis and inductance changes was observed. Figure 7C displays the inductance changes of the sensor under different normal loads. The results demonstrate the sensor's capability to perform both static and dynamic measurements. The linear response of the sensor to varying shear loads is illustrated in Figure 7D. The sensor, with its highest sensitivity of 2.63% kPa^{-1} (910 nH/N, 0-1 N) for normal pressure sensing and 2.80% kPa^{-1} (4.67 μH/N) for shear sensing, significantly outperforms inductive sensors based on other mechanisms [Figure 1D, Supplementary Note 1, Supplementary Figure 1, and Supplementary Table 1]. Notably, the sensing performance (with 500 μm c-PCL) is designed to meet the requirement of the RGO application. For applications requiring different sensing performances, such as a larger sensing range, a smaller pore size can be chosen for c-PCL. For example, the sensor with 200 μm c-PCL exhibits a sensing range of 0-12.6 N and a sensitivity of 1.11% kPa^{-1} (383 nH/N, 0-2 N) for normal pressure sensing and 1.18% kPa^{-1} (1.96 μH/N) for shear sensing, which is also significantly sensitive than other inductive sensors.

As shown in Supplementary Figure 13A and B, the average response times under normal and shear loads are 21 and 20 ms, respectively, which are comparable to the response time of human skin (30-50 ms)[65]. Here, the response time is defined as the time interval between 10% and 90% of the steady-state values[66].

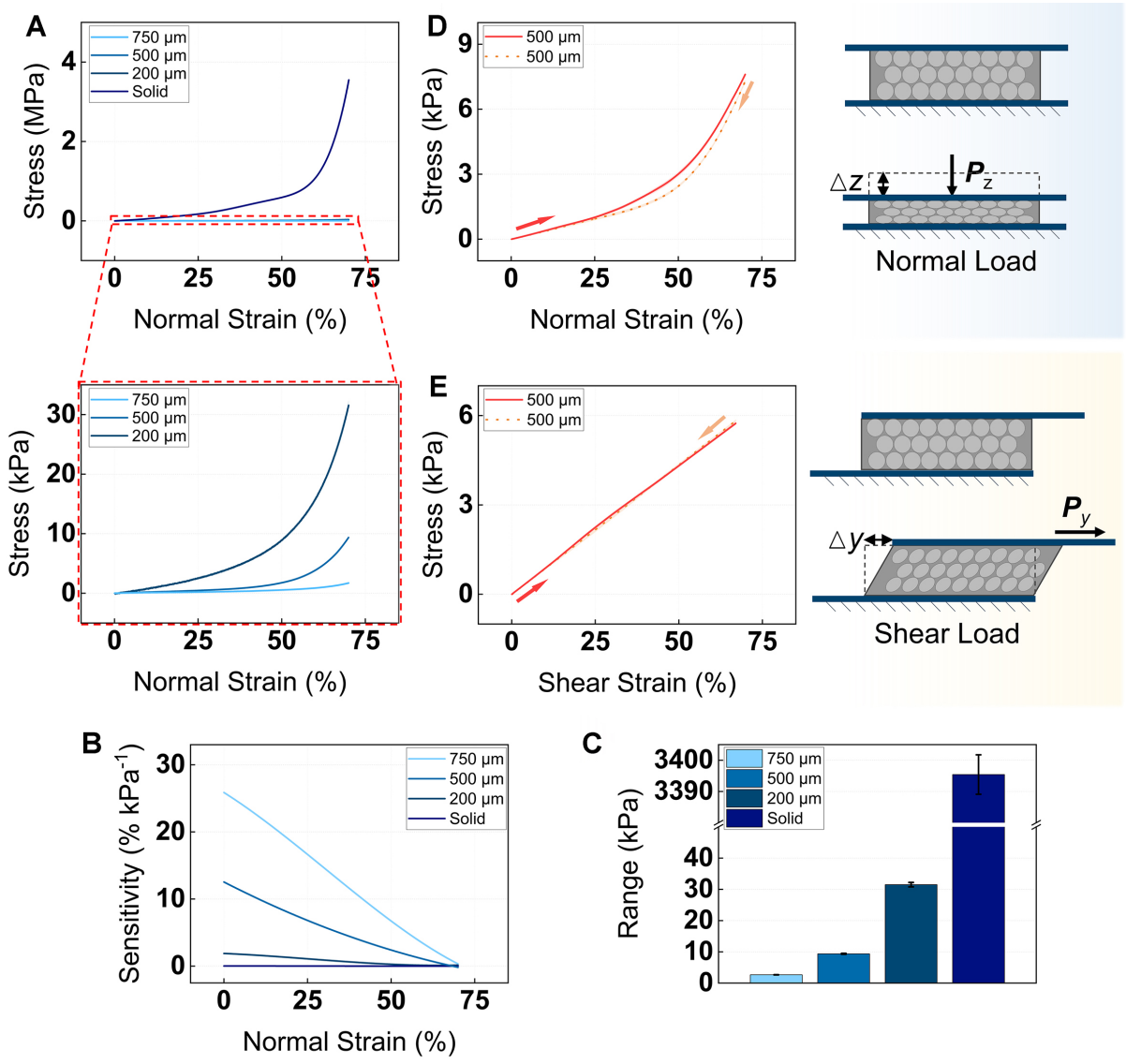

Figure 6. Characterizations of the c-PCL. (A) Strain-stress curves of c-PCLs with different pore sizes; (B) Tactile sensitivity and (C) sensing range under normal loads for c-PCLs with different pore sizes; (D) Compressive and (E) shear stress-strain curves of the c-PCL and the schematic illustration of the testing conditions. c-PCL: porous compressible layer (with AgNWs embedded) serving as a conductive medium.

The recovery times are 32 ms under normal loads and 24 ms under shear loads. Supplementary Figure 13C and D illustrates the reliability of the sensor, demonstrating that under varying rates of applied normal and shear loads, the DTTS exhibits consistent and reliable sensing performance. Figure 7E and F illustrates the inductance changes of the DTTS under different repetitive normal and shear loads. To further validate the sensor's cyclic stability, 1,000 cycles of loading and unloading were conducted [Figure 7G and H]. These results confirm the robust performance of the DTTS under repeated mechanical loadings. The flexibility of the device was also tested [Supplementary Figure 14]. Under bending, the sensor exhibited only a slight performance reduction (less than 5%).

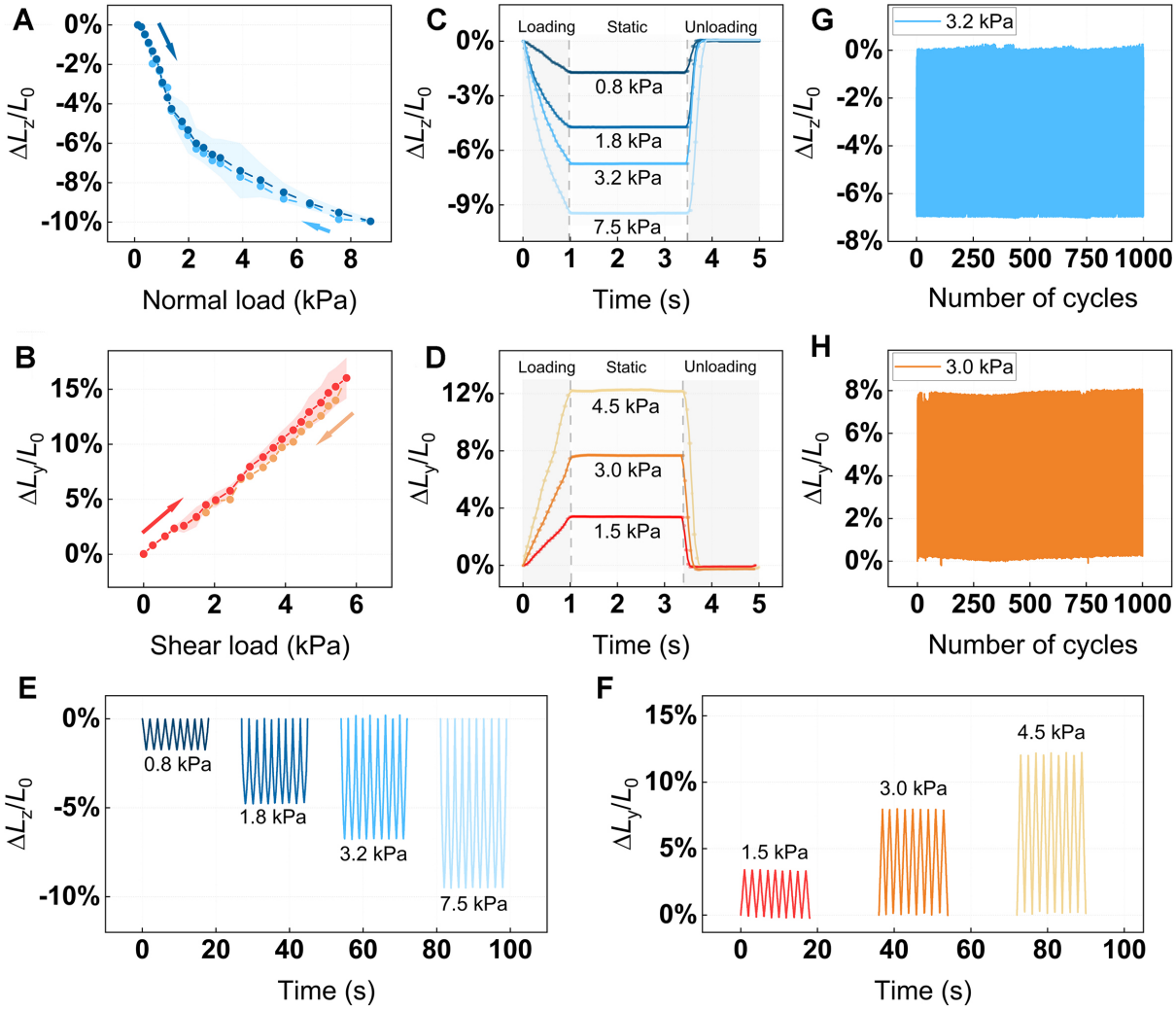

Figure 7. Tactile sensing performance of the DTTS. (A) Inductance changes along the *z*-axis when a normal load is applied. (B) Inductance changes along the *y*-axis when a shear load is applied. Inductance changes under different (C) normal and (D) shear loadings. Inductance changes under repetitive (E) normal and (F) shear loadings. Cyclic testing over 1,000 cycles under (G) a normal loading of 3.2 kPa and (H) a shear loading of 3 kPa. DTTS: Dual tri-axial tactile sensors.

Proof-of-concept demonstrations

Demonstration in real-time tactile monitoring

RGOs are primarily used to assist people with partial or total loss of lower limb function caused by spinal cord injuries, spina bifida, or neuromuscular dystrophy[67,68]. The movement between the RGO and the skin generates significant pressure and friction, known as the "piston effect". Due to the patient's impaired sensation, these forces often lead to skin ulcers, irritations, and wounds, thereby increasing the risk of infections and resulting in greater reduced mobility and even permanent disability[69]. Monitoring both normal and shear stresses between the RGO and the skin is therefore essential for assessing skin conditions and early detection of pressure ulcers that compromise the patient's quality of life.

To demonstrate the sensor's capability of real-time monitoring of normal and shear stresses in daily activities, the DTTS was attached between a user's upper leg and the thigh cuff of an RGO [Supplementary Figure 15]. The schematic of the overall system is shown in Supplementary Figure 16. The sensor served to monitor the normal and shear loads exerted by the RGO on the skin as the user was involved in different

daily activities, such as sitting, standing, and walking. Tactile loads corresponding to these activities include normal, static shear, and dynamic shear loads, respectively [Figure 8A].

The top four curves in Figure 8B represent inductance changes from four channels of the inductive sensor across various activities. The bottom curve indicates the calculated normal and shear loads associated with the user's movements along the *x*-, *y*-, and *z*-axes. The results reveal that during sitting, there was primarily normal load due to the tight attachment of the RGO. When the user shear force along the *y*-axis was also present due to relative movement between the user's leg and RGO. As the user started walking, the shear force exhibited a repetitive dynamic pattern that matched the user's walking dynamics. Notably, the shear load along the *x*-axis was minimal compared to forces in other axes, as there was almost no relative movement between the user's leg and the RGO along the *x*-axis. The normal load remained fairly constant, with slight fluctuations caused by the muscle expansion and contraction during walking, which altered the distance between the skin and the orthosis. These observations confirm that the sensor is able to effectively monitor 3-axial tactile information during daily activities. The real-time tactile sensing provides important insight into the normal and shear loads between the orthosis and the user's skin, which is essential to ensure the orthosis is properly worn for the prescribed time and to prevent potential skin damage and pressure ulcers due to excessive loads during utilization[70].

Demonstration of the sensors' stability to environmental objects

Excellent stability and resistance to environmental objects are crucial for the daily use of tactile sensors. For instance, when tactile sensors are mounted between the RGO and the skin of a user, the sensors inevitably encounter different objects. As an example, to assess its stability to environmental objects involved in RGO application, the sensor was exposed to different materials including human skin, silicones, plastics, water, and alcohol [Figure 8C (i)]. As shown in Figure 8C (ii), the DTTS exhibits excellent stability to these environmental objects, with only marginal variations in inductance against the baseline inductance (recorded when the sensor was placed in the air, free from any environmental interference). Since resistive and piezoelectric sensors have drawbacks in their sensing mechanisms, as discussed in the previous section, capacitive tactile sensors, by contrast, offer low hysteresis and a wide dynamic range. However, their susceptibility to environmental contaminants, including oil, water, and dust, can interfere with signal outputs. Thus, capacitive sensors were selected for the comparison of stability to environmental objects. A comparative analysis was conducted on the capacitive tactile sensor of the same geometry and materials. The capacitor sensor consists of two parallel plate electrodes based on silver ink and a PCL dielectric sandwiched in between. When exposed to different materials, the capacitive sensor displays much more obvious variations, originating from its high sensitivity to the dielectric properties of surrounding materials[71].

The superior stability and resistance to environmental objects of the DTTS stems from the nature of magnetic fields, which are barely impacted by environmental interferences (e.g., water, plastic, alcohol, and human body). Although human tissues are conductive, the low conductivity is insufficient to generate a significant inductance change that can negatively affect the sensor's stability. This feature ensures that the DTTS is highly reliable in wearable applications.

CONCLUSION

This work introduces the design, fabrication, and optimization of dual-mechanism, highly sensitive, soft tri-axial inductive sensors that are capable of detecting both static and dynamic normal and shear loads. The sensor coils are optimized to achieve a uniform magnetic field that significantly improves the sensitivity to normal/shear loads and the linearity for shear sensing. Fabrication of the coil is enabled by a precise laser

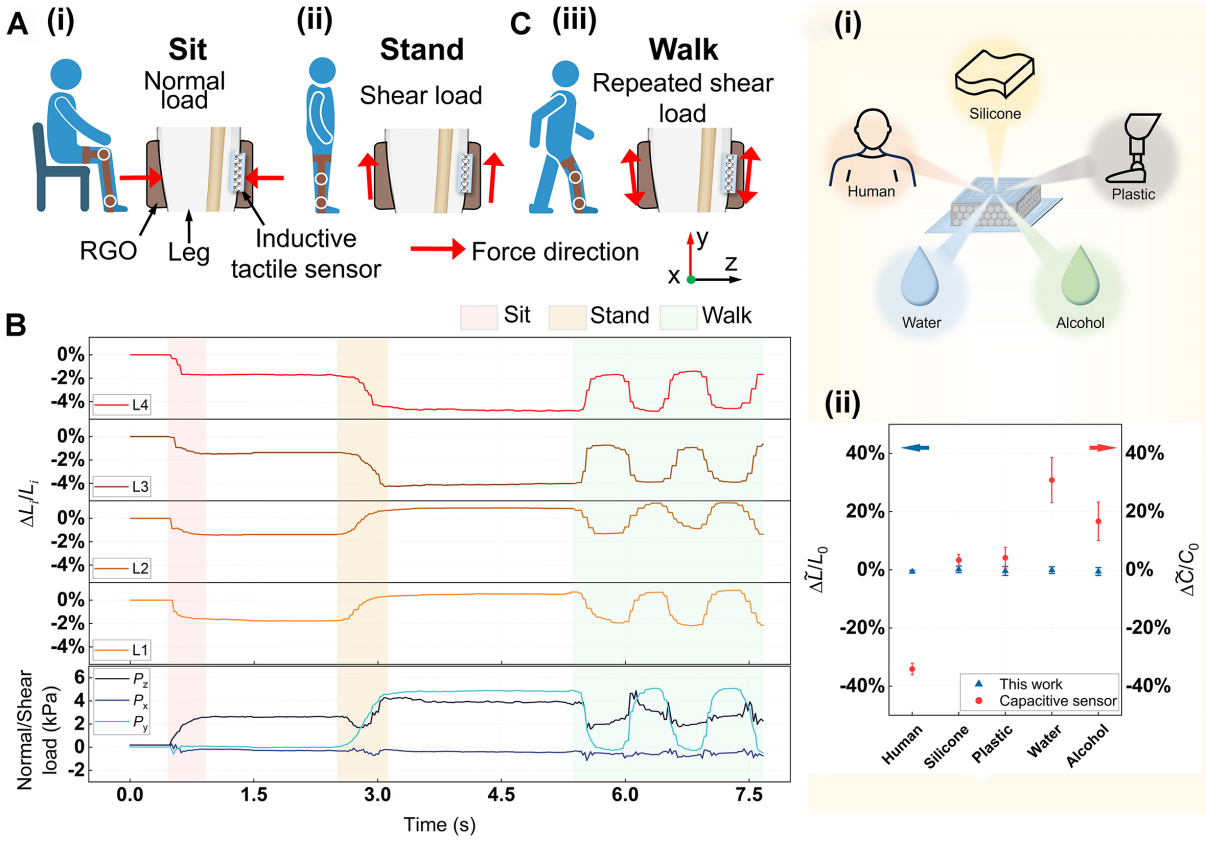

Figure 8. Proof-of-concept demonstrations of the sensor. (A) Demonstration of real-time tactile sensing: Schematic illustrations depicting the primary sensing mode when a user is (i) sitting, (ii) standing, and (iii) walking. There are also normal loads in standing and walking scenarios, which are not shown for clarity purposes; (B) Measured 4-channel inductance changes of the DTTS during the above three activities, and the corresponding calculated normal and shear loads. $\Delta L_i / L_i$ indicates the inductance change of each channel, *i* is from 1 to 4; (C) Demonstration of the stability of the sensor to environmental contaminants: (i) Illustrations of common environmental objects. (ii) Variations of sensing signals of the DTTS and a capacitive sensor when different environmental objects are in proximity. $\Delta\tilde{L}$ is the inductance change of the inductive sensor and $\Delta\tilde{C}$ is the capacitance change of the capacitive sensor when the sensors are exposed to different environmental objects. L_0 is the inductance of the inductive sensor and C_0 is the capacitance of the capacitive sensor when the sensors are free from any environmental interference. DTTS: Dual tri-axial tactile sensors; RGO: reciprocating gait orthosis.

patterning technique based upon a pulsed wave picoseconds laser source. By employing the principles of the Biot-Savart law and EC effect and a tunable PCL, the sensor achieves a sensitivity of 2.63% kPa^{-1} (910 nH/N) for normal loads and 2.80% kPa^{-1} (4.67 μH/N) for shear loads, surpassing existing inductive sensors. Constructed from fully soft materials, the developed sensor demonstrates excellent flexibility, enabling it to conform to curved surfaces, such as human legs and RGO. The sensor is capable of detecting tri-axial forces between the leg and the RGO during everyday activities. In addition, the sensor exhibits a superior robustness against environmental objects.

DECLARATIONS

Authors' contributions

Conceptualization and methodology: Chen, S.; Yao, S.
Sensor fabrication: Chen, S.; Li, S.; Zheng, Y.; Fong, B.
Data acquisition: Chen, S.; Li, S.; Zheng, Y.

Data analysis: Chen, S.; Li, S.; Zheng, Y.; Li, Y.; Dong, P.; Hwang, D.; Yao, S.
Manuscript writing and editing: Chen, S.; Yao, S.; Zheng, Y.; Hwang, D.
Funding acquisition and project supervision: Yao, S.

Availability of data and materials

The data that support the findings of this study are available from the corresponding author upon reasonable request.

Financial support and sponsorship

This material was based upon work supported by the National Science Foundation under Award (No. ECCS-2238363). Yao, S. would like to acknowledge the support from the start-up fund at Stony Brook University and the Stony Brook Trustees Faculty Awards Program.

Conflicts of interest

All authors declared that there are no conflicts of interest.

Ethical approval and consent to participate

All subjects provided informed consent.

Consent for publication

Not applicable.

REFERENCES

1. Seminara, L.; Gastaldo, P.; Watt, S. J.; Valyear, K. F.; Zuher, F.; Mastrogiovanni, F. Active haptic perception in robots: a review. *Front. Neurorobot.* **2019**, *13*, 53. DOI PubMed PMC
2. Nemah, M. N.; Low, C. Y.; Aldulaymi, O. H.; Ong, P.; Ismail, A. E.; Qasim, A. A. A review of non-invasive haptic feedback stimulation techniques for upper extremity prostheses. *IJIE.* **2019**, *11*, 299-326. DOI
3. Lim, S.; Son, D.; Kim, J.; et al. Transparent and stretchable interactive human machine interface based on patterned graphene heterostructures. *Adv. Funct. Mater.* **2015**, *25*, 375-83. DOI
4. Flesher; SN; Downey, J. E.; Weiss, J. M.; et al. A brain-computer interface that evokes tactile sensations improves robotic arm control. *Science* **2021**, *372*, 831-6. DOI PubMed PMC
5. Santhanam, G.; Ryu, S. I.; Yu, B. M.; Afshar, A.; Shenoy, K. V. A high-performance brain-computer interface. *Nature* **2006**, *442*, 195-8. DOI PubMed
6. Chen, S.; Chen, Y.; Yang, J.; Han, T.; Yao, S. Skin-integrated stretchable actuators toward skin-compatible haptic feedback and closed-loop human-machine interactions. *npj. Flex. Electron.* **2023**, *7*, 235. DOI
7. Chen, S.; Yu, L.; Shen, W.; et al. Multimodal 5-DOF stretchable electromagnetic actuators toward haptic information delivery. *Adv. Funct. Mater.* **2024**, *34*, 2314515. DOI
8. Brookhuis, R.; Lammerink, T.; Wiegerink, R.; de, B. M.; Elwenspoek, M. 3D force sensor for biomechanical applications. *Sens. Actuators. A. Phys.* **2012**, *182*, 28-33. DOI
9. Xu, H.; Chai, G.; Zhang, N.; Gu, G. Restoring finger-specific tactile sensations with a sensory soft neuroprosthetic hand through electrotactile stimulation. *Soft. Sci.* **2022**, *2*, 19. DOI
10. Xu, Y.; Yu, S.; Liu, L.; et al. In-Sensor touch analysis for intent recognition. *Adv. Funct. Mater.* **2024**, *34*, 2411331. DOI
11. Huang, Z.; Yu, S.; Xu, Y.; et al. In-sensor tactile fusion and logic for accurate intention recognition. *Adv. Mater.* **2024**, *36*, e2407329. DOI PubMed
12. Chen, Z.; Lin, W.; Zhang, C.; et al. Multifunctional and reconfigurable electronic fabrics assisted by artificial intelligence for human augmentation. *Adv. Fiber. Mater.* **2024**, *6*, 229-42. DOI
13. Kaltenbrunner, M.; Sekitani, T.; Reeder, J.; et al. An ultra-lightweight design for imperceptible plastic electronics. *Nature* **2013**, *499*, 458-63. DOI PubMed
14. Choi, G.; Jang, H.; Oh, S.; et al. A highly sensitive and stress-direction-recognizing asterisk-shaped carbon nanotube strain sensor. *J. Mater. Chem. C.* **2019**, *7*, 9504-12. DOI

15. Shi, M.; Zhang, J.; Chen, H.; et al. Self-powered analogue smart skin. *ACS. Nano.* **2016**, *10*, 4083-91. DOI PubMed
16. Ham, J.; Huh, T. M.; Kim, J.; et al. Porous dielectric elastomer based flexible multiaxial tactile sensor for dexterous robotic or prosthetic hands. *Adv. Mater. Technol.* **2023**, *8*, 2200903. DOI
17. Johansson, R. S.; Flanagan, J. R. Coding and use of tactile signals from the fingertips in object manipulation tasks. *Nat. Rev. Neurosci.* **2009**, *10*, 345-59. DOI PubMed
18. Sun, K.; Ko, H.; Park, H. H.; et al. Hybrid architectures of heterogeneous carbon nanotube composite microstructures enable multiaxial strain perception with high sensitivity and ultrabroad sensing range. *Small* **2018**, *14*, e1803411. DOI PubMed
19. Chen, S.; Bai, C.; Zhang, C.; et al. Flexible piezoresistive three-dimensional force sensor based on interlocked structures. *Sens. Actuators. A. Phys.* **2021**, *330*, 112857. DOI
20. Kwon, S.; Kim, S.; Kim, I.; Hong, Y. K.; Na, S. Direct 3D printing of graphene nanoplatelet/silver nanoparticle-based nanocomposites for multiaxial piezoresistive sensor applications. *Adv. Mater. Technol.* **2019**, *4*, 1800500. DOI
21. Tibrewala, A.; Hofmann, N.; Phataralaoha, A.; Jäger, G.; Büttgenbach, S. Development of 3D force sensors for nanopositioning and nanomeasuring machine. *Sensors* **2009**, *9*, 3228-39. DOI PubMed PMC
22. Ting, Y.; Suprapto; Nugraha, A.; Chiu, C.; Gunawan, H. Design and characterization of one-layer PVDF thin film for a 3D force sensor. *Sens. Actuators. A. Phys.* **2016**, *250*, 129-37. DOI
23. Zhu, Y.; Jiang, S.; Xiao, Y.; Yu, J.; Sun, L.; Zhang, W. A flexible three-dimensional force sensor based on PI piezoresistive film. *J. Mater. Sci. Mater. Electron.* **2018**, *29*, 19830-9. DOI
24. Jones, D.; Wang, H.; Alazmani, A.; et al. A soft multi-axial force sensor to assess tissue properties in realtime. In *2017 IEEE/RSJ International Conference on Intelligent Robots and Systems (IROS)*, Vancouver, Canada, September 24-28, 2017; Publisher: IEEE; pp 5738-43. DOI
25. Nakashima, R.; Takahashi, H. Multi-axial tactile sensor using standing lig cantilevers on polyimide film. In *2022 IEEE 35th International Conference on Micro Electro Mechanical Systems Conference (MEMS)*, Tokyo, Japan, January 9-13, 2022; Publisher: IEEE; pp 688-90. DOI
26. Kim, K.; Ahn, J.; Jeong, Y.; Choi, J.; Gul, O.; Park, I. All-soft multiaxial force sensor based on liquid metal for electronic skin. *Micro. Nano. Syst. Lett.* **2021**, *9*, 126. DOI
27. Kim, K.; Park, J.; Suh, J.; Kim, M.; Jeong, Y.; Park, I. 3D printing of multiaxial force sensors using carbon nanotube (CNT)/thermoplastic polyurethane (TPU) filaments. *Sens. Actuators. A. Phys.* **2017**, *263*, 493-500. DOI
28. Wu, J.; Pancham, P. P.; Hsu, T.; et al. Capacitive tactile sensor with stacked structure and hybrid fabrication for multiaxial force decoupling. In *2022 IEEE Sensors*, Dallas, USA, October 30-November 2, 2022; Publisher: IEEE; pp 1-3. DOI
29. Zheng, H.; Jin, Y.; Wang, H.; Zhao, P. DotView: A low-cost compact tactile sensor for pressure, shear, and torsion estimation. *IEEE. Robot. Autom. Lett.* **2023**, *8*, 880-7. DOI
30. Aksoy, B.; Digumarti, K. M.; Shea, H. Soft monolithic shielded sensors to measure shear and normal forces for local slip detection. *Adv. Mater. Technol.* **2024**, *9*, 2400486. DOI
31. Hu, H.; Zhang, C.; Pan, C.; et al. Wireless flexible magnetic tactile sensor with super-resolution in large-areas. *ACS. Nano.* **2022**, *16*, 19271-80. DOI PubMed
32. Yan, Y.; Hu, Z.; Yang, Z.; et al. Soft magnetic skin for super-resolution tactile sensing with force self-decoupling. *Sci. Robot.* **2021**, *6*, eabc8801. DOI PubMed
33. Wang, H.; Jones, D.; de, B. G.; et al. Design and characterization of tri-axis soft inductive tactile sensors. *IEEE. Sensors. J.* **2018**, *18*, 7793-801. DOI
34. Yao, S.; Ren, P.; Song, R.; et al. Nanomaterial-enabled flexible and stretchable sensing systems: processing, integration, and applications. *Adv. Mater.* **2020**, *32*, e1902343. DOI PubMed
35. ATI Industrial Automation. Measure all six components of force and torque in a compact, rugged transducer. Available from: https://www.ati-ia.com/Products/ft/sensors.aspx. [Last accessed on 10 Jan 2025].
36. FUTEK Advanced Sensor Technology. Multi-axis sensors. Available from: https://www.futek.com/store/multi-axis-sensors. [Last accessed on 10 Jan 2025].
37. Wang, L.; Jones, D.; Chapman, G. J.; et al. An inductive force sensor for in-shoe plantar normal and shear load measurement. *IEEE. Sensors. J.* **2020**, *20*, 13318-31. DOI
38. Wang, C.; Wang, T.; Liu, B.; Tian, F.; Lu, X. Metal thickness measurement system based on a double-coil eddy-current method with characteristic ratio detection. *IEEE. Trans. Ind. Electron.* **2023**, *70*, 12904-12. DOI
39. Chen, X.; Ding, T. Flexible eddy current sensor array for proximity sensing. *Sens. Actuators. A. Phys.* **2007**, *135*, 126-30. DOI
40. Kawasetsu, T.; Niiyama, R.; Kuniyoshi, Y. Flexible and soft inductive tri-axis tactile sensor using liquid metal as sensing target. In *2019 IEEE SENSORS*, Montreal, Canada, October 27-30, 2019; Publisher: IEEE; pp 1-4. DOI
41. Dong, P.; Song, Y.; Yu, S.; et al. Electromyogram-based lip-reading via unobtrusive dry electrodes and machine learning methods. *Small* **2023**, *19*, e2205058. DOI PubMed
42. Liu, J. M. Simple technique for measurements of pulsed Gaussian-beam spot sizes. *Opt. Lett.* **1982**, *7*, 196-8. DOI PubMed
43. Yao, S.; Zhou, W.; Hinson, R.; et al. Ultrasoft porous 3D conductive dry electrodes for electrophysiological sensing and myoelectric control. *Adv. Mater. Technol.* **2022**, *7*, 2101637. DOI PubMed PMC
44. Kim, J. O.; Kwon, S. Y.; Kim, Y.; et al. Highly ordered 3D microstructure-based electronic skin capable of differentiating pressure, temperature, and proximity. *ACS. Appl. Mater. Interfaces.* **2019**, *11*, 1503-11. DOI PubMed

45. Wang, H.; Kow, J.; Raske, N.; et al. Robust and high-performance soft inductive tactile sensors based on the Eddy-current effect. *Sens. Actuators. A. Phys.* **2018**, *271*, 44-52. DOI
46. Wang, H.; Liu, Y.; Li, W.; et al. Design of ultrastable and high resolution eddy-current displacement sensor system. In *IECON 2014-40th Annual Conference of the IEEE Industrial Electronics Society*, Dallas, USA, October 29-November 1, 2014; Publisher: IEEE; pp 2333-39. DOI
47. Liyuan, Y.; Shushu, L.; Pingjuan, N.; Hao, S.; Run, M.; Zheng, C. Novel square spiral Coil for achieving uniform Distribution of magnetic field. *IOP. Conf. Ser. Earth. Environ. Sci.* **2019**, *332*, 042005. DOI
48. Peters, C.; Manoli, Y. Inductance calculation of planar multi-layer and multi-wire coils: an analytical approach. *Sens. Actuators. A. Phys.* **2008**, *145-146*, 394-404. DOI
49. Rosa, E. B. The self and mutual inductances of linear conductors. Available from: https://nvlpubs.nist.gov/nistpubs/bulletin/04/nbsbulletinv4n2p301_a2b.pdf. [Last accessed on 10 Jan 2025].
50. Wang, H.; Totaro, M.; Veerapandian, S.; et al. Folding and bending planar coils for highly precise soft angle sensing. *Adv. Mater. Technol.* **2020**, *5*, 2000659. DOI
51. Kawasetsu, T.; Horii, T.; Ishihara, H.; Asada, M. Flexible tri-axis tactile sensor using spiral inductor and magnetorheological elastomer. *IEEE. Sensors. J.* **2018**, *18*, 5834-41. DOI
52. Zhu, Y.; Zhou, W.; Yao, S. Gas permeable, ultrathin, stretchable epidermal electronic devices and related methods. US 20220340726A1, 2022. Available from: https://patents.google.com/patent/US20220340726A1/en. [Last accessed on 10 Jan 2025].
53. Yao, S.; Yang, J.; Poblete, F. R.; Hu, X.; Zhu, Y. Multifunctional electronic textiles using silver nanowire composites. *ACS. Appl. Mater. Interfaces.* **2019**, *11*, 31028-37. DOI PubMed
54. Trotec. Laser cutting and engraving machine Speedy Series. Available from: https://www.troteclaser.com/en-us/laser-machines/laser-engravers-speedy-series. [Last accessed on 10 Jan 2025].
55. Yeh, S.; Fang, W. Inductive micro tri-axial tactile sensor using a CMOS chip with a coil array. *IEEE. Electron. Device. Lett.* **2019**, *40*, 620-3. DOI
56. Wattanasarn, S.; Noda, K.; Matsumoto, K.; et al. 3D flexible tactile sensor using electromagnetic induction coils. In *2012 IEEE 25th International Conference on Micro Electro Mechanical Systems (MEMS)*, Paris, France, January 29-February 2, 2012; Publisher: IEEE; pp 488-91. DOI
57. Du, L.; Zhu, X.; Zhe, J. An inductive sensor for real-time measurement of plantar normal and shear forces distribution. *IEEE. Trans. Biomed. Eng.* **2015**, *62*, 1316-23. DOI PubMed
58. Hamaguchi, S.; Kawasetsu, T.; Horii, T.; et al. Soft inductive tactile sensor using flow-channel enclosing liquid metal. *IEEE. Robot. Autom. Lett.* **2020**, *5*, 4028-34. DOI
59. Casanova, J. J.; Low, Z. N.; Lin, J.; et al. Transmitting coil achieving uniform magnetic field distribution for planar wireless power transfer system. In *2009 IEEE Radio and Wireless Symposium*, San Diego, USA, January 18-22, 2009; Publisher: IEEE; pp 530-3. DOI
60. Xu, Q.; Hu, Q.; Wang, H.; Mao, Z.; Sun, M. Optimal design of planar spiral coil for uniform magnetic field to wirelessly power position-free targets. *IEEE. Trans. Magn.* **2021**, *57*, 1-9. DOI
61. Li, S.; Niu, P.; Yu, L.; et al. Design method of primary transmitting coil for realizing large uniform magnetic field distribution. In *2018 3rd International Conference on Mechanical, Control and Computer Engineering (ICMCCE)*, Huhhot, China, September 14-16, 2018; Publisher: IEEE; pp 112-6. DOI
62. Diao, Y.; Shen, Y.; Gao, Y. Design of coil structure achieving uniform magnetic field distribution for wireless charging platform. In *2011 4th International Conference on Power Electronics Systems and Applications*, Hong Kong, China, June 8-10, 2011; Publisher: IEEE; pp 1-5. DOI
63. Gefen, A.; Ousey, K. COVID-19: pressure ulcers, pain and the cytokine storm. *J. Wound. Care.* **2020**, *29*, 540-2. DOI PubMed
64. StatPearls Publishing. Pressure ulcer. Available from: https://www.ncbi.nlm.nih.gov/books/NBK553107/. [Last accessed on 10 Jan 2025].
65. Gu, M.; Zhao, B.; Gao, J.; et al. Nested-cell architecture and molecular surface modification enabled 10 megapascals range high sensitivity flexible pressure sensors for application in extreme environment. *Adv. Funct. Mater.* **2024**, *34*, 2400494. DOI
66. Yao, S.; Zhu, Y. Wearable multifunctional sensors using printed stretchable conductors made of silver nanowires. *Nanoscale* **2014**, *6*, 2345-52. DOI PubMed
67. Arazpour, M.; Bani, M. A.; Hutchins, S. W. Reciprocal gait orthoses and powered gait orthoses for walking by spinal cord injury patients. *Prosthet. Orthot. Int.* **2013**, *37*, 14-21. DOI PubMed
68. Lourenco, L.; Blanes, L.; Salomé, G. M.; Ferreira, L. M. Quality of life and self-esteem in patients with paraplegia and pressure ulcers: a controlled cross-sectional study. *J. Wound. Care.* **2014**, *23*, 331-4,336. DOI PubMed
69. Lyder C.; E., A. Pressure Ulcers: A Patient Safety Issue. In *Patient Safety and Quality: An Evidence-Based Handbook for Nurses*; Hughes R.G., Eds.; Vol. 3; Rockville (MD): Agency for Healthcare Research and Quality (US); 2008, Chapter 12. PubMed
70. Devanand, D. B.; Kedgley, A. E. Objective methods of monitoring usage of orthotic devices for the extremities: a systematic review. *Sensors* **2023**, *23*, 7420. DOI PubMed PMC
71. Cheng, A. J.; Wu, L.; Sha, Z.; et al. Recent advances of capacitive sensors: materials, microstructure designs, applications, and opportunities. *Adv. Mater. Technol.* **2023**, *8*, 2201959. DOI